Exciton-phonon coupling and band-gap renormalization in monolayer WSe_2

Himani Mishra,[1] Anindya Bose,[1] Amit Dhar,[2] and Sitangshu Bhattacharya[1,*]
[1]*Nanoscale Electro-Thermal Laboratory, Department of Electronics and Communication Engineering, Indian Institute of Information Technology–Allahabad, Uttar Pradesh 211015, India*
[2]*Department of Information Technology, Indian Institute of Information Technology–Allahabad, Uttar Pradesh 211015, India*

(Received 4 May 2018; revised manuscript received 19 June 2018; published 31 July 2018)

Using a fully *ab initio* methodology, we demonstrate how the lattice vibrations couple with neutral excitons in monolayer WSe_2 and contribute to the nonradiative excitonic lifetime. We show that only by treating the electron-electron and electron-phonon interactions at the same time is it possible to obtain an unprecedented agreement of the zero- and finite-temperature optical gaps and absorption spectra with the experimental results. The bare energies were calculated by solving the Kohn-Sham equations, whereas G_0W_0 many-body perturbation theory was used to extract the excited-state energies. A coupled electron-hole Bethe-Salpeter equation was solved incorporating the polaronic energies to show that it is the in-plane torsional acoustic phonon branch that contributes mostly to the *A* and *B* exciton buildup. We find that the three *A*, *B*, and *C* excitonic peaks exhibit different behavior with temperature, displaying different nonradiative linewidths. There is no considerable transition in the strength of the excitons with temperature, but the *A* exciton remains dark in comparison with the *C* exciton. Further, all the excitonic peaks redshift as temperature rises. Renormalization of the bare electronic energies by phonon interactions and anharmonic lattice thermal expansion causes a decreasing band gap with increasing temperature. The zero-point energy renormalization (31 meV) is found to be entirely due to the polaronic interaction with a negligible contribution from lattice anharmonicities. These results may have a profound impact on electronic and optoelectronic device technologies based on these monolayers.

DOI: 10.1103/PhysRevB.98.045143

I. INTRODUCTION

The transition-metal dichalcogenide (TMDC) family and their monolayer (ML) films have distinguished themselves as a perfect platform to understand various finite-temperature quantum many-body phenomena [1–4]. Among them, the optical-absorption spectrum contains information about the fundamental band-gap and band-edge energies. When a photon with energy larger than this gap is incident, an electron changes its state from a valence band to a conduction band, thereby leaving a hole in the former. If the external screening between them is weak, then this particle hole pairs for a sufficiently long time via Coulombic attraction. In ML films, this pairing is equivalent to a two-dimensional hydrogen-like atom with quantized energy states. Fingerprints of such quasiparticles (QPs) or excitons can be obtained from peaks in the optical-absorption spectra determined by nonlinear two-photon photoluminescence (2PPL) and angle-resolved photoemission spectroscopy (ARPES) [5–10] measurements. The photon energies corresponding to these peaks are of central importance as they determine the condition of maximum photocarrier generation. However, the exciton energies as well as the widths of the peaks in the absorption spectra are strongly affected by the presence of lattice vibrations. Determination of the exciton lifetime at nonzero temperatures, therefore, stands as a bottleneck to understand the exciton-phonon dynamics in optical devices based on these materials.

Intrinsic exfoliated ML WSe_2, when illuminated by such photons, displays the sharpest and brightest neutral excitonic ground-state peaks *A* and *B* at 1.65 and 2.05 eV, respectively, with a giant binding energy of 0.37 eV at 300 K [8,11]. These, along with other excited excitonic states, can be well captured from 2PPL measurements, done along Γ-**K** and Γ-**K**′ of the Brillouin zone (BZ), confirming that ML WSe_2 possesses a direct optical band gap. Conclusive evidence about the giant valence spin-orbit splitting (SOS) of 513 ± 10 meV at **K** and **K**′ arising due to the lack of crystal inversion symmetry can also be obtained from the ARPES measurements [12]. As it is difficult to capture the conduction band or its splitting profile directly from ARPES, one may looks for the presence of a dark exciton. In these MLs, a dark exciton is formed when an electron pairs to a hole with antiparallel spin (intravalley) and parallel spin (intervalley). Fortunately, due to the presence of time-reversal (TR) symmetry [$E(\mathbf{K}\uparrow) = E(\mathbf{K}'\downarrow)$], the spin and momenta at these two valleys are coupled [2,13,14]. This means that at **K** the top two valence bands separately are spin-up and -down, while the two lowest conduction bands separately are spin-down and -up, respectively. A complementary scenario is then obtained at **K**′ by exploiting the TR symmetry. Therefore, a dark exciton can only form when a hole at the top valence band at **K** pairs with an electron at the lowest conduction band of **K** (intravalley) and **K**′ (intervalley) [15,16]. Conversely, since a bright exciton is formed only when an electron pairs to a hole with a parallel spin (intravalley) and an antiparallel spin (intervalley), the difference in the bright-dark excitonic energies provides the split energy difference between the conduction bands. This is found to be 30 ± 5 meV for ML

*Author to whom all correspondence should be addressed: sitangshu@iiita.ac.in

WSe_2 [17]. In MoX_2 (X = Se, Te, and S) MLs, this energy is found to be negative, suggesting that the dark excitons house themselves in higher energies, beyond the first ground-state bright exciton.

Many-body perturbation theory (MBPT) has been quite successful in explaining the absorption spectra and excitonic energies, and it has shown convincing results done on Si and other hexagonal family members [18–23]. However a quantitative understanding about the exciton-phonon coupling in ML WSe_2 still needs to be addressed. In particular, it is the excitonic nonradiative widths that are most difficult to capture through experiments, and therefore we use the MBPT as a tool to calculate it. Here we demonstrate the integrated effect of the electron-electron and electron-phonon interactions on the electronic and optical properties of intrinsic ML WSe_2. We show that under such a scenario, there is an unprecedented agreement of the zero- and finite-temperature optical gaps and absorption spectra with the experimental results. We start with an evaluation of bare electronic energies by first solving the Kohn-Sham set of equations using density-functional theory (DFT). MBPT is then used to compute the QP energies on the top of this by switching on the dynamic electron-electron correlation. This eventually fixes the energy gap, which is otherwise grossly underestimated using only DFT. To get the renormalized excitonic energies, absorption spectra, and lifetimes, we solve a coupled electron-hole Bethe-Salpeter equation (BSE) that includes the polaronic energies extracted from density-functional perturbation theory (DFPT) calculations giving an excellent description of the phonon frequencies and coupling strengths. The methodology adopted here is therefore fully *ab initio* and demands no external parameters.

II. THEORY

In intrinsic crystals, there are three types of coupling that mostly controls the temperature-dependent absorption spectra. The first one is the coupling between electronic and atomic degrees of freedom. MBPT provides useful information about the zero-point renormalization (ZPR) of the widths not present in the bare-particle states $|n,\mathbf{k}\rangle$. The electron-phonon (EP) matrix elements [24]

$$g^{\mathbf{q}\lambda}_{n'n\mathbf{k}} = \sum_{\alpha s}\langle n,\mathbf{k}|\nabla_{\alpha s}\phi_{\rm scf}|n',\mathbf{k}+\mathbf{q}\rangle \times \sum_{\mathbf{q}\lambda}\left(\frac{1}{2M_s\omega_{\mathbf{q}\lambda}}\right)^{\frac{1}{2}} e^{-iq\tau_s}\epsilon^*\left(\frac{\mathbf{q}\lambda}{s}\right) \quad (1)$$

describe the electron-scattering probability amplitudes from $\mathbf{k}$ to $\mathbf{k}+\mathbf{q}$ due to the emission or absorption of a phonon with transferred momenta $\mathbf{q}$ in branch λ. Here, the self-consistent potential $\phi_{\rm scf}$ is first obtained by calculating the charge densities from DFT. DFPT is then used to calculate the first-order derivative of $\phi_{\rm scf}$ with respect to atomic displacements α and consequently the dynamical matrices. For this, the entire BZ is sampled by a number of random $\mathbf{q}$ points. Instead of assigning a regular $\mathbf{q}$-grid sampling, this method gives additional flexibility of employing new weight $\frac{1}{N_q}$ implicitly in the electron-phonon self-energy integral and is therefore mainly used [25–27]. τ_s is the location of mass M of the sth atomic species in the unit cell, and $\epsilon^*(\frac{\mathbf{q}\lambda}{s})$ are the polarization vectors. The states $|\mathbf{k}+\mathbf{q}\rangle$ are finally obtained via a non-self-consistent calculation done on the same regular grid (see the Appendix for computational details). Using the Matsubara Green's function, one can write the polaronic self-energies after an analytic continuation on the real axis as [24]

$$\sum^{\rm Fan}_{n\mathbf{k}}(\omega) = \sum_{n'\mathbf{q}\lambda}\left|g^{\mathbf{q}\lambda}_{n'n\mathbf{k}}\right|^2\left[\frac{N(\omega_{\mathbf{q}\lambda})+1-f_{n'\mathbf{k}-\mathbf{q}}}{\omega-\epsilon_{n'\mathbf{k}-\mathbf{q}}-\omega_{\mathbf{q}\lambda}-i0^+} + \frac{N(\omega_{\mathbf{q}\lambda})+f_{n'\mathbf{k}-\mathbf{q}}}{\omega-\epsilon_{n'\mathbf{k}-\mathbf{q}}+\omega_{\mathbf{q}\lambda}-i0^+}\right]. \quad (2)$$

Here N and f are the phonon and electron distribution functions, respectively, and 0^+ is used to make the contour integral vanish over the half-circle of the upper half-plane. The second-order EP matrix elements stem from the renormalized screening due to the atomic motion and are calculated by invoking translational invariance symmetry. The frequency-independent self-energies can then be written as [28]

$$\sum^{\rm DW}_{n\mathbf{k}} = -\sum_{\mathbf{q}\lambda}\sum_{n'}\frac{\Lambda^{\mathbf{q}\lambda,-\mathbf{q}\lambda}_{nn'\mathbf{k}}}{\epsilon_{n\mathbf{k}}-\epsilon_{n'\mathbf{k}}}[2N(\omega_{\mathbf{q}\lambda})+1], \quad (3)$$

in which

$$\Lambda^{\mathbf{q}\lambda,-\mathbf{q}\lambda}_{nn'k} = \frac{1}{2}\sum_{s}\sum_{\alpha,\beta}\frac{\epsilon^*_\alpha\left(\frac{\mathbf{q}\lambda}{s}\right)\epsilon_\beta\left(\frac{-\mathbf{q}\lambda}{s}\right)}{2M_s\omega_{\mathbf{q}\lambda}}\langle n\mathbf{k}+\mathbf{q}+\mathbf{q}'\,|\nabla_{\alpha s}\nabla_{\beta s}\phi_{\rm scf}|n\mathbf{k}\rangle$$

are the corresponding second-order couplings.

Equations (2) and (3) are the Fan and Debye-Waller (DW) self-energies used to compute the electronic Green's function $G^{\rm EP}_{n\mathbf{k}}(\omega) = [\omega-\epsilon_{n\mathbf{k}}-\sum^{\rm Fan}_{n\mathbf{k}}(\omega)-\sum^{\rm DW}_{n\mathbf{k}}(\omega)]^{-1}$. The real part of this pole is the renormalized QP energies while the imaginary part corresponds to the polaronic lifetime. Assuming that the bare energies $\epsilon_{n\mathbf{k}}$ are far from the poles of the real or imaginary Fan self-energies, one does a Taylor's expansion about $\epsilon_{n\mathbf{k}}$, and a renormalization weight factor $Z^{\rm EP}_{n\mathbf{k}}$ ($0 < Z^{\rm EP}_{n\mathbf{k}} < 1$) is therefore assigned to each $|n,\mathbf{k}\rangle$ state resulting in

$$\Delta E^{\rm EP}_{n\mathbf{k}} - \epsilon_{n\mathbf{k}} \approx Z^{\rm EP}_{n\mathbf{k}}{\rm Re}\left[\sum^{\rm Fan}_{n\mathbf{k}}(\omega)+\sum^{\rm DW}_{n\mathbf{k}}(\omega)\right] \quad (4)$$

with $Z^{\rm EP}_{n\mathbf{k}} = [1-\frac{\partial}{\partial\omega}{\rm Re}\sum^{\rm Fan}_{n\mathbf{k}}(\omega)|_{\omega=\epsilon_{n\mathbf{k}}}]^{-1}$. Equation (4) is the dynamical HAC (Heine, Allen, and Cardona) [29] theory and represents a finite zero-point energy even when $T \to 0$ K. This way the uncertainty principle is also satisfied, with the added advantage that the exciton absorption spectra do not demand any fitting-broadening parameter. When $\epsilon_{n\mathbf{k}}$ are very far from the poles of real and imaginary Fan self-energies such that $\frac{\partial}{\partial\omega}{\rm Re}\sum^{\rm Fan}_{n\mathbf{k}}(\omega) = \frac{\partial}{\partial\omega}{\rm Im}\sum^{\rm Fan}_{n\mathbf{k}}(\omega) = 0$, only virtual electronic scatterings are allowed, and Taylor's expansion is computed up to zeroth order [28]. This is known as the static limit or the on-the-mass-shell approach ($Z_{n\mathbf{k}} \to 1$). The imaginary part of $G^{\rm EP}_{n\mathbf{k}}(\omega)$ also reflects the spectral function (SF) $\mathsf{A}^{\rm EP}_{n\mathbf{k}}(\omega) = \frac{1}{\pi}|{\rm Im}G^{\rm EP}_{n\mathbf{k}}(\omega)|$. Weak coupling results in a sharp SF centered at $\Delta E^{\rm EP}_{n\mathbf{k}}$. As the coupling gets stronger, the Lorentzian SF peak starts becoming more asymmetric and dwarf. Physically, $Z^{\rm EP}_{n\mathbf{k}}$ signifies the fraction of the positive charge that a bare

electron takes away from the QP cloud and forms satellite peaks. Comparing the energy difference between the main and the satellite peak with the Debye energy, the validity of the QP assumption can be verified. Equation (4) can also be used to understand which phonon mode actually contributed to the nonradiative excitonic linewidth. This can be calculated from the Eliashberg function for each state $|n,\mathbf{k}\rangle$ [30],

$$g^2_{n\mathbf{k}}F(\omega)=\sum_{q\lambda}\frac{\partial E^{\mathrm{EP}}_{n\mathbf{k}}}{\partial N(\omega_{q\lambda})}\delta(\omega-\omega_{q\lambda}), \tag{5}$$

and mapping it to the corresponding phonon dispersion.

In addition to EP coupling, lattice thermal expansion (LTE) also modifies the bare-particle energies and can be of the same order compared to the former [31]. The energy renormalization within a variable volume quasiharmonic approximation (QHA) can be obtained by minimizing the Helmholtz free energy [32]

$$F(\{a_j\},T)-\epsilon(\{a_j\})=\sum_{q,\lambda}\frac{\hbar\omega_{q,\lambda}(\{a_j\})}{2}+k_BT\sum_{q,\lambda}\ln\left[1-\exp\left(-\frac{\hbar\omega_{q,\lambda}(\{a_j\})}{k_BT}\right)\right]. \tag{6}$$

The first-term on the right is the vibrational zero-point energy, while the second term on the left is the DFT bare energy performed with respect to the geometrical degrees of freedom a_j and the sums extending the BZ. Equation (4) when combined with Eq. (6) gives the net ZPR due to LTE and EP coupling.

The second coupling is the dynamic long range electron-electron (EE) correlation and is responsible for opening the QP electronic energy gap or simply the G_0W_0 gap. Within the linear-response theory, the diagonal matrix element of the dynamic correlational part of the self-energy in the plane-wave basis set can be written as [30]

$$\langle n\mathbf{k}|\sum(\omega)|n\mathbf{k}\rangle=i\sum_m\int_{\mathrm{BZ}}\frac{d\mathbf{q}}{(2\pi)^3}\sum_{\mathbf{GG}'}\frac{4\pi}{|\mathbf{q}+\mathbf{G}|^2}\rho_{nm}\times(\mathbf{k},\mathbf{q},\mathbf{G})\rho^*_{nm}(\mathbf{k},\mathbf{q},\mathbf{G})\int d\omega' G^0_{m\mathbf{k}-\mathbf{q}}(\omega-\omega')\varepsilon^{-1}_{\mathbf{GG}'}(\mathbf{q},\omega') \tag{7}$$

in which m spans all the occupied to unoccupied bands, and $\mathbf{G}$ are the G vectors of the plane waves in the Fourier transformed plane. G^0 is the single-particle Green's propagator, and $\varepsilon^{-1}_{\mathbf{GG}'}$ is the microscopic frequency-dependent dielectric function, which can be efficiently calculated using the Godby-Needs plasmon-pole approximation model [33] to solve the dynamic screening W at the random-phase approximation (RPA) level. By including the static exchange part of the self-energy, the QP energies can be obtained as $\Delta E^{\mathrm{EE}}_{n\mathbf{k}}=\epsilon_{n\mathbf{k}}+Z^{\mathrm{EE}}_{n\mathbf{k}}\langle\psi_{n\mathbf{k}}|\sum(\epsilon_{n\mathbf{k}})-V_{\mathrm{xc}}|\psi_{n\mathbf{k}}\rangle$, in which V_{xc} is obtained by solving the Kohn-Sham equations. It is then clear that the corrections to the band gap due to the EE correlation are orders of magnitude higher than the EP interactions. Similar to the EP case, the SF here is again the imaginary Green's propagator that can be captured well by ARPES measurements.

The third is the dynamic long-range electron-hole (e-h) coupling describing the two-particle Green's propagator. The corresponding equation of motion is the BSE [34]. Under the frozen-atom (FA) approximation (i.e., no atomic vibrations), the Bethe-Salpeter (BS) Hamiltonian is a Hermitian matrix in the e-h pair basis with eigenstates $|\varphi_{\mathrm{FA}}(T)\rangle$. The excitonic eigenenergies can then be obtained by formulating the corresponding Hamiltonian in the form [18]

$$H^{\mathrm{FA}}_{ee',hh'}=(E_e-E_h)\delta_{eh,e'h'}+(f_e-f_h)K_{ee',hh'}, \tag{8}$$

in which $K_{ee',hh'}$ is a BS kernel and is the sum of a repulsive (positive) bare Coulomb exchange term and an attractive (negative) direct e-h screened interaction term. The former stems from the variation of the Hartree potential and is responsible for spin-singlet/triplet splitting, while the latter is long-range and responsible for the formation of excitonic bound states. $(E/f)_{e/h}$ are the corresponding quasi-e/h energies and Fermi occupation numbers. When lattice vibrations and LTE effects are present, E_e and E_h broaden to ΔE_e and ΔE_h, respectively, and they make the BS Hamiltonian a non-Hermitian operator. However, in most semiconductors the QP corrections due to LTE are much less compared to $\Delta E^{\mathrm{EP}}_{nk}$, except in some special cases resulting in an anomalous band-gap dependency on temperature [31]. This is still not reported in monolayer TMDCs. Relaxing only LTE contributions, therefore, the excitonic energy eigenvalues can be written in the form [18]

$$E_\varphi(T)=\langle\varphi(T)|H^{\mathrm{FA}}|\varphi(T)\rangle+\sum_{e,h}\left|A^\varphi_{e,h}(T)\right|^2\times[\Delta E_e(T)-\Delta E_h(T)]. \tag{9}$$

It is then straightforward to extract the real and imaginary parts from Eq. (9) as

$$\mathrm{Re}[\Delta E_\varphi(T)]=\langle\varphi(T)|H^{\mathrm{FA}}|\varphi(T)\rangle-\langle\varphi_{\mathrm{FA}}|H^{\mathrm{FA}}|\varphi_{\mathrm{FA}}\rangle+\int d\omega\,\mathrm{Re}[g^2F_\varphi(T)]\left[N(\omega,T)+\frac{1}{2}\right] \tag{10}$$

and

$$\mathrm{Im}[E_\varphi(T)]=\int d\omega\,\mathrm{Im}[g^2F_\varphi(T)]\left[N(\omega,T)+\frac{1}{2}\right]. \tag{11}$$

The difference $g^2F_\varphi(T)=\sum_{e,h}|A^\varphi_{eh}(T)|^2[g^2F_e(\omega)-g^2F_h(\omega)]$ represents the exciton-phonon coupling function and $\Delta E_\varphi(T)=E_\varphi(T)-E^{\mathrm{FA}}_\varphi$. The temperature-dependent macroscopic dielectric function in the long-wavelength limit is therefore

$$\varepsilon_M(\omega,T)=-\frac{8\pi}{\Omega}\sum_\varphi|O_\varphi(T)|^2\mathrm{Im}[\omega-E_\varphi(T)]^{-1}. \tag{12}$$

$\mathrm{Im}\varepsilon_M(\omega,T)$ defines the complete absorption spectra with the exciton oscillator strength $O_\varphi(T)=\langle n\mathbf{k}|\exp(i\boldsymbol{\kappa}\cdot\mathbf{r})\{[|\varphi(T)\rangle-|\varphi^{\mathrm{FA}}(T)\rangle]\}$ in which $\boldsymbol{\kappa}$ is the electric polarization vector direction and Ω is the volume. A more elaborate theoretical treatment on Hedin's GW formalism and BSE can be found elsewhere [34–36].

III. RESULTS AND DISCUSSIONS

A. Bare and G_0W_0 energies

WSe_2 belong to the space group $P63/mmc$. To replicate a full all-electron potential within the atoms, a norm-conserving

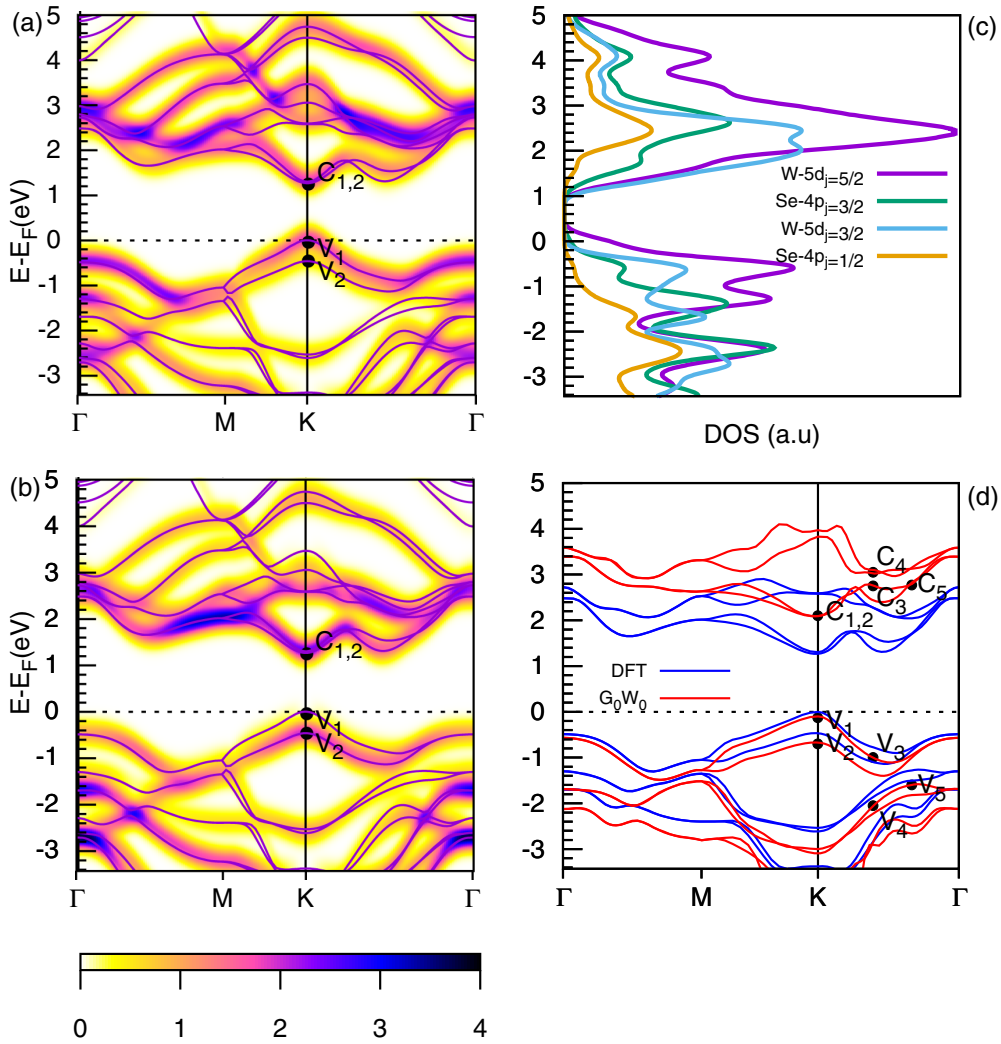

FIG. 1. (a,b) Bare electronic energy dispersions in ML WSe_2 along the BZ. Spin is resolved and projected onto each state with ($l = 2$) and exhibiting $m_s = +\frac{1}{2}$ occupancy in (a) and $-\frac{1}{2}$ occupancy in (b). These occupancies are shown by darker areas. The partial density of states is shown in (c) for $5d$ and $4p$ orbitals of W and Se, respectively, mostly influencing the total angular momenta. The antiparallel spins are clearly visible near the bottom of the conduction band and the top of the valence band. Excited-state G_0W_0 dispersions are shown in (d) with a direct band gap of 2.19 eV. C and V represent electronic transitions during optical excitations.

and fully relativistic pseudopotential was first generated [37]. The $5s$, $5p$, and $4f$ semicore orbitals were included for W along with $5d$ and $6s$ valence electrons. The PBE exchange-functional was selected because of two reasons: (a) after testing with a variety of other functionals (see the Appendix for computational details), the convergence of the lattice constant here is found to be in good agreement compared with the experimental data (with a slight overestimation of 0.04 Å), and (b) an exchange-functional like the LDA tends to underestimate the electron-phonon interactions by 30% [38].

In Figs. 1(a) and 1(b), V_1 and V_2 at K are the split valence bands (Zeeman-like) due to the spin-orbit coupling (SoC) in which both of them are mainly populated with $5d$ orbital electrons from the W atom. The spin occupancy due to the L-S (L denotes the orbital angular momentum and S denotes the spin angular momentum) coupling results in an orbital angular momentum ($l = 2$) and spin quantum number $m_s = +\frac{1}{2}$ for V_1 and $-\frac{1}{2}$ for V_2, respectively. The giant spin-orbit splitting between these two is found to be $|\Delta E_V^{SoC}| = 466$ meV, while the energy difference of V_1 between the K-Γ direction is -492 meV. Further, the SoC results in a splitting of conduction bands C_1 and C_2 at K with $|\Delta E_C^{SoC}| = 37$ meV. The lowest valley conduction band in the K-Γ direction is almost degenerate with C_1 at K and is located above 44 meV [for a magnified diagram, see Fig. S2(b) in the Supplemental Material [39]]. These band edges, therefore, result in a direct bare energy gap (E_g) of almost 1.26 eV. The partial density of states contributed by different atomic orbitals and spins is shown in Fig. 1(c), in which the conduction bands C_1 and C_2 are mainly found to build up by $5d_{j=\frac{3}{2}}$ (spin-down) and $5d_{j=\frac{5}{2}}$ (spin-up) of the W atom, respectively. The scenario is the opposite in the top two valence bands, where V_1 and V_2 are mainly found to build up by $5d_{j=\frac{5}{2}}$ (spin-up) and $5d_{j=\frac{3}{2}}$ (spin-down) of the W atom, respectively. This antiparallel spin occupancy in both split valence and conduction bands is due to the broken inversion symmetry. Interestingly, in the case of ML MoX_2 (X = S and Se), parallel spin polarizations in V_1, C_1 and V_2, C_2 are found [16,40].

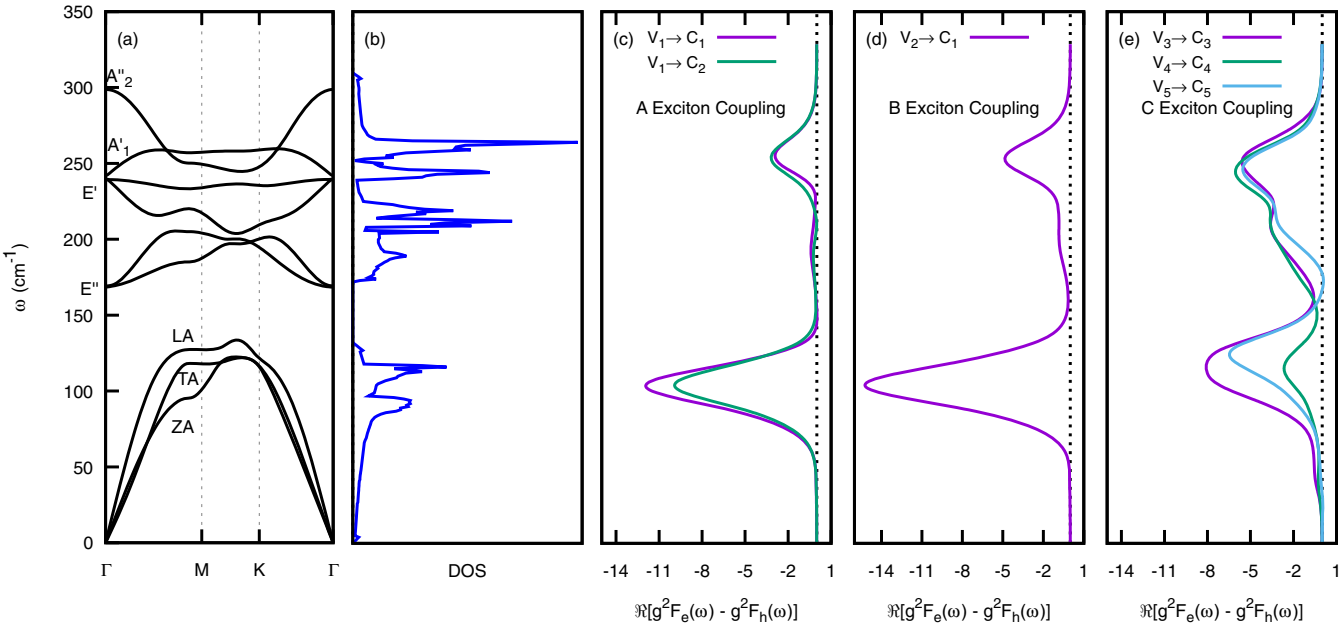

FIG. 2. Phonon (a) dispersion and (b) density of states in ML WSe_2 along the BZ. The real part of the difference between the conduction- and valence-band Eliashberg functions along the lattice frequency of vibrations calculated for (c) (V_1, C_1), (V_1, C_2) (responsible for A-exciton buildup), (d) (V_2, C_1) (responsible for B-exciton buildup), and (e) (V_3, C_3), (V_4, C_4), and (V_5, C_5) (responsible for C-exciton buildup). All the differences are negative suggesting a band-gap shrinkage as temperature rises.

To capture the excitation results, the excited-state correction G_0W_0 method was employed (see the Appendix for computational details). The inclusion of the dynamic EE correlation [Eq. (7)] then opens up E_g to 2.19 eV, which is in excellent agreement with the reported range of 2.02-2.35 ± 0.2 eV for exfoliated WSe_2 MLs [8,10]. Comparing both the G_0W_0 and DFT results, it is evident that the difference $Z^{\rm EE}_{n\mathbf{k}}\langle\psi_{n\mathbf{k}}|\sum(\epsilon_{n\mathbf{k}}) - V_{\rm xc}|\psi_{n\mathbf{k}}\rangle$ essentially provides a rigid energy shift only (with $\mathrm{Re}Z^{\rm EE} = 77\%$ and 76% for V_1 and C_1, respectively), showing that these dynamic EE-correlated QP corrections are rather weakly dependent on **k**-vector directions. It is also evident that the change in the energies of the unoccupied states after G_0W_0 corrections is considerably larger when compared to the occupied ones, and it is mainly due to the change in the binding energies, which results in an increase in the valence-band width. In the case of unoccupied states, the low-lying conduction bands formed now have larger QP corrections as they are highly localized in nature, supporting the fact that self-interaction errors in the DFT are severe for localized states, therefore producing an infinite lifetime. Further, the two low-lying nondegenerate conduction bands at K after G_0W_0 corrections acquire a 40 meV separation. This is in excellent agreement with the experimentally evaluated splitting of the conduction bands (30 ± 5 eV) found by probing the dark excitonic states [17]. The almost degenerate satellite bands obtained in Kohn-Sham calculations are now lifted up to 393.8 meV while the valence-band splitting opens up to $|\Delta E_v^{\mathrm{SoC},G_0W_0}| = 572$ meV. Interestingly, there are also recent reports about the indirect band gap found in chemical vapor deposition (CVD) -grown ML WSe_2 [41,42]. By using scanning tunneling spectroscopy, Zhang *et al.* [41] reported an indirect QP gap of 2.12 ± 0.06 eV in the Γ-**K** direction. They also reported a direct QP gap at the **K**-**K** transition of 2.20 ± 0.10 eV, nearly degenerate with the indirect gap. However, Zhang *et al.* [41] also suspected that this indirect band gap might have occurred because their WSe_2 was grown on graphite with a Moiré pattern that imposed additional periodicity, thereby modifying the QP band structure. Hsu *et al.* [42] investigated the spatially resolved PL from a ML WSe_2-MoS_2 lateral heterojunction (HJ) with inherent nonuniform strain distribution. They first demonstrated PL from strained MoS_2 in WSe_2-MoS_2 lateral HJs as a model system to extract the energy differences between the direct and indirect gaps in ML MoS_2. Then they demonstrated the study of $MoSe_2$-WSe_2 lateral HJs and showed that unstrained ML WSe_2 is actually an indirect gap material. It is therefore interesting to observe from the above references that ML WSe_2 prepared by mechanical exfoliation demonstrates a direct band gap, while ML WSe_2 prepared by the CVD technique results in an indirect band gap. In any case, we find that our *ab initio* energies and absorption spectra are in excellent agreement with the case of exfoliated ML WSe_2.

B. DFPT and electron-phonon self-energies

DFPT is now used to understand the lattice vibrations and EP self-energies. Bulk WSe_2 belongs to the $D_{4h}(\bar{6}2m)$ symmorphic group. In the case of ML film, the group symmetry reduces to $D_{3h}(\bar{6}2m)$, where the nine modes at Γ decompose into four irreducible representations A_2'', E', E'', and A_1'. The dispersion and the density of states have been exhibited in Figs. 2(a) and 2(b). Modes E', E'', and A_1' are equivalent to E_{2g}, E_{1g}, and A_{1g} in the bulk case, respectively. Both the in-plane longitudinal acoustic (LA) mode and the out-of plane optical (ZO) mode A_2'' are IR (infrared) -active. The ZA and TA motions E' are both degenerate, IR-, and Raman-active.

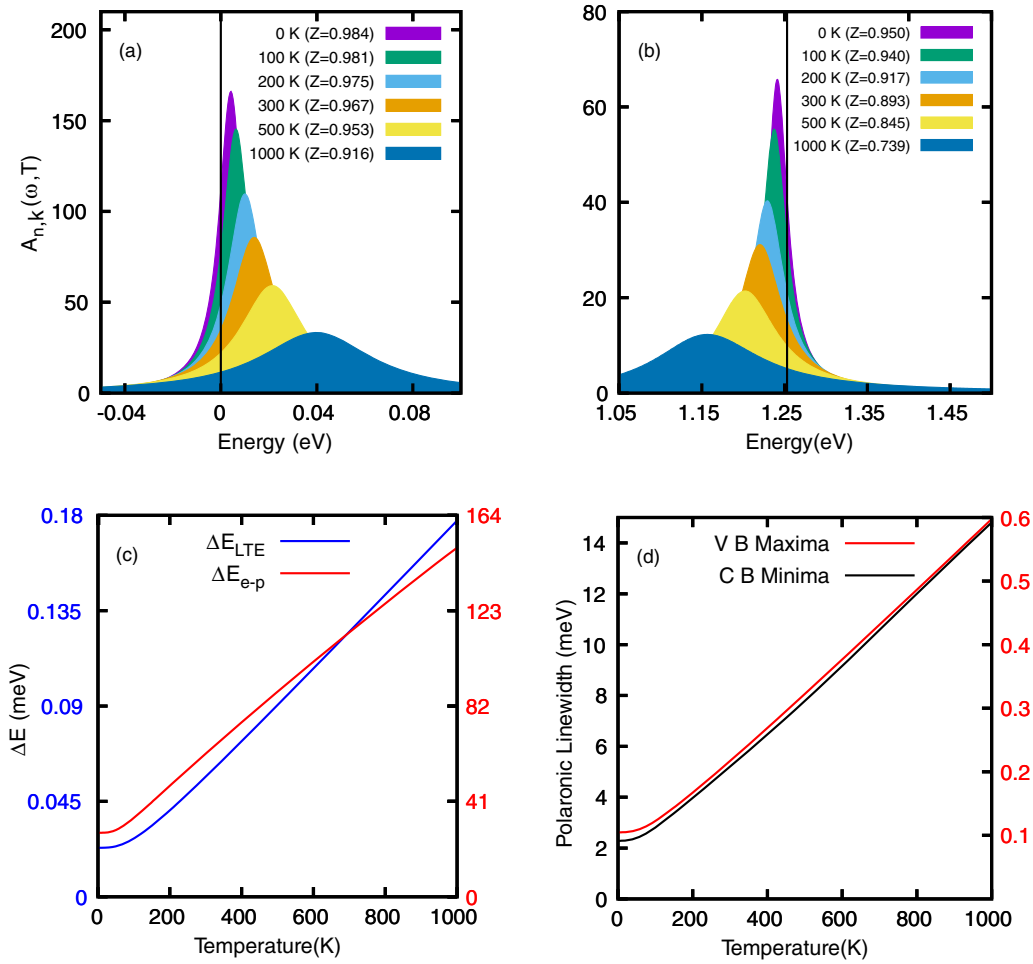

FIG. 3. (a,b) Spectral functions at the top valence band and lowest conduction band at different temperatures, respectively. The vertical line marks the bare energy values. The Lorentzian shape broadens as temperature rises with respective blue- and redshifting of the valence and conduction band. (c) Zero-point energy as a function of temperature due to the electron-phonon renormalization (red curve) and lattice anharmonicity (blue curve) representing a band-gap reduction with temperature. (d) Band-resolved polaronic linewidth as a function of temperature. Only the valence-band maxima and conduction-band minima linewidth at the K point is shown.

The two midfrequency modes E'' are in-plane, degenerate, and only Raman-active. Further, the two modes E' in the lower optical regions are degenerate with both IR- and Raman-active modes, while the out-of phase ZO modes A_1' (Se-Se) and A_2'' (Se-W-Se) are IR- and Raman-active, respectively. The first- and second-order E-P matrix elements [Eqs. (2) and (3)] were then calculated by sampling the entire BZ into 113 random transferred-momenta grids and 288 random **k** points, respectively. We did not impose electron-phonon-mediated spin mixing in any bands as it is found to be insignificant in similar structures [27]. We reserve our discussions on the Eliashberg functions shown in Figs. 2(c)–2(e) in conjunction with the exciton formations in subsequent paragraphs. The SFs of valence and conduction bands at K are shown in Figs. 3(a) and 3(b). Since SFs are proportional to the full width at half-maximum of the polaronic linewidths, a sharper SF would then mean a more stable electronic state, i.e., a finite yet longer lifetime. As the temperature increases, the SF broadens in energy, thereby interacting a great deal with phonons and leading to a faster transition to another excitonic state of similar energy. The SF broadening of the electronic states at 0 K can now be calculated from Eq. (4), in which the peak corresponds to the zero-point energy. One can then see a generic trend of redshifting (conduction) and blueshifting (valence) of the peaks with temperature. Such a trend leads to the well-known band-gap shrinkage and is shown in Fig. 3(c). A careful analysis on the polaronic corrections to the width is shown in Fig. 3(d). The width varies slowly at lower temperature but increases linearly at higher temperature. This behavior is due to the renormalization of the electronic energies by acoustic phonons, which is also exhibited by the Eliashberg functions shown in Fig. 2(c), where the contribution from optical phonons is much less for the above-mentioned bands. The residual width is the zero-point correction and is found to be smaller for the top valence band but an order of magnitude larger for the bottom conduction band at K. This is in accordance with the uncertainty principle, as a smaller width results in a longer lifetime. We find that by using a fully dynamic self-energy computation, the conduction and valence bands shrink by 2% and 0.1%, respectively, leading to a correction of 31 meV below the bare gap of 1.26 eV. The zero-temperature QP weights for the conduction and valence

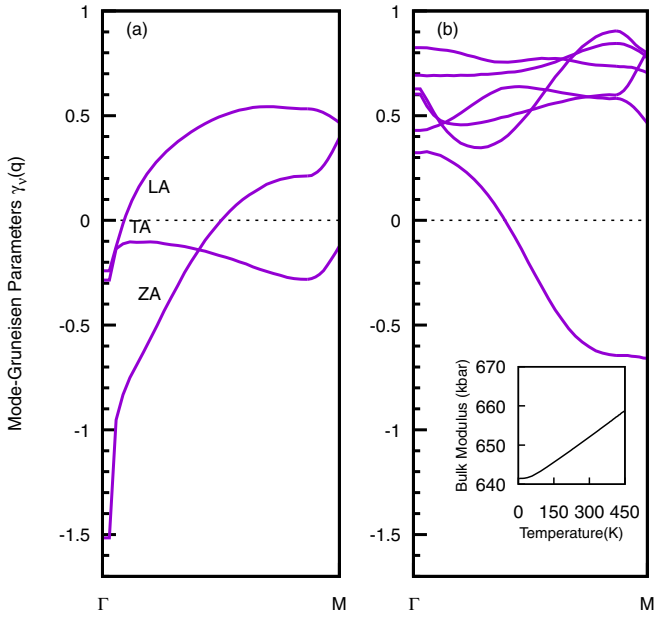

FIG. 4. The mode-dependent Grüneisen parameter along the Γ-M BZ zone. The lowest three acoustic modes are shown in (a) while the optical modes are shown in (b). A negative $\gamma_\lambda(\mathbf{q})$ is obtained in the ZA mode at Γ resulting in a lattice thermal contraction. The inset shows the variation of the bulk modulus with respect to the temperature.

bands are found to be 95% and 98%, respectively, leading to the conclusion of the good QP state. The SF peaks of the latter are much larger in magnitude than those of the former due to the larger widths. Increasing the temperature to 1000 K reduces the QP weights to 73% and 91%, respectively, which calls into question the validity of the QP assumptions for the conduction band. However, even at this temperature we did not find any appreciable emergence of secondary peaks as in the case of *trans*-polyacetylene [43].

C. Lattice anharmonicities and the ZPR

To understand the band-gap reduction due to LTE [Eq. (6)], a variable volume QHA computation was also carried out. The lattice anharmonicities are captured by altering only the in-plane lattice constants to two geometries centered about the relaxed one with a strain of ±0.01 Å. Once the Helmholtz free energy is minimized, the corresponding zero-point energy is extracted by fitting into the second-order Birch-Murnaghan equation of state [32].

To understand the anharmonicities that might contribute to the ZPR at a nonzero temperature, we have additionally computed the Grüneisen parameter $\gamma_\lambda(\mathbf{q}) = -\frac{\partial \ln \omega_{q\lambda}}{\partial \ln V}$ for each of the phonon modes along the Γ-M direction of the BZ. The lowest three acoustic modes are shown in Fig. 4(a) whereas the rest of the optical modes are displayed in Fig. 4(b). Immediately by looking at the center Γ of the BZ, we find that the out-of-plane ZA mode appears to be the dominant mode that dips to a much more negative value, resulting in a lattice thermal contraction at lower temperature. The optical modes that are not yet excited are clear signatures of positive $\gamma_\lambda(\mathbf{q})$. As the temperature rises, the dormant optical modes wake up and lattice expansion occurs. The lattice contraction in this case, however, is indeed small and was captured by Çakır *et al.* [44]. Since there is no stacking layer involved in ML WSe_2, a positive strain then increases the ZA frequency of vibrations, resulting in the well-known membrane effect [45]. This was observed earlier in graphene [32] and recently in silicene, germanene, and blue phosphorene [46]. Interestingly, we obtained a $\gamma_{A_{1g}}(\Gamma) = 0.69$ that is close to the experimentally evaluated value of 0.55 [47]. The computation of ZPR uses the bulk modulus B_T, and therefore in the inset of Fig. 4(b) the variation of the same with temperature is shown. We find a monotonically increasing behavior with a room temperature $B_T = 65.2$ GPa, which is a little less than its corresponding bulk value of 72 GPa [47]. The influence of LTE on band-gap reduction was shown in Fig. 3(c). The anharmonic contribution is small, as expected due to the larger atomic masses, but it does not show any decreasing (anomalous) behavior. We thus find that the gap shrinkage is mainly due to the electron-phonon interactions. Table I summarizes the ZPR obtained in this work with other ML TMDCs and bulk members. Comparing with the ML counterpart, we see that the ZPR decreases as the weight of the formula units increases, which is consistent since heavier atoms vibrate less.

TABLE I. ZPR of ML TMDCs and other materials.

Structure	ZPR (meV)
ML WSe_2	31 (this work)
Black phosphorus [31]	20
trans-polyacetylene [43]	40
ML MoS_2 [27]	75
Si [48]	123
SiC [48]	223
Polyethylene [43]	280
Diamond [49]	622

D. Absorption spectra and excitonic states

The absorption spectra at different temperatures have been computed using a coupled BSE and are shown in Fig. 5. Both the resonant and antiresonant electron-hole pairs were included in the BS kernel since the omission of the latter, known as the Tamm-Dancoff approximation [50], underestimates the collective density oscillations, which consist also of the electron-hole pairs. The absorption spectra at 300 K have been exhibited in Fig. 5(a), which contains the polaronic widths and quasienergies at each state $|n, \mathbf{k}\rangle$ as well as the dynamic long-range electron-electron gap correction. To include this G_0W_0 correction, we use a scissor operator of 0.928 eV and a linearly fitted conduction- and valence-band stretching of 1.134 and 1.069 eV, respectively (see Fig. S3 in the Supplemental Material [39]). The vertical arrows represent the bare energy gap 1.26 eV and the G_0W_0 gap 2.19 eV. A static screening was then computed to build up the BS kernel. The inset in Fig. 5(a) shows an enlarged view for comparison of our work with the reported experimental results [8]. The A and B excitons are found to be located at 1.61 and 2.06 eV compared with the experimental values of 1.65 and 2.08 eV. The ground-state exciton

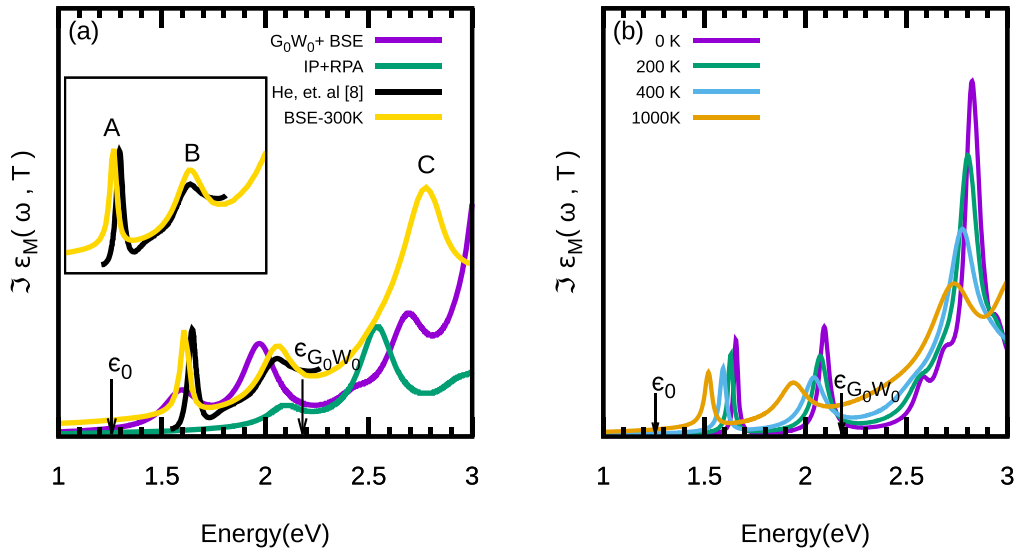

FIG. 5. BSE is used to extract the temperature-dependent absorption spectra as a function of photon energy at (a) 300 K. The peaks A, B, and C correspond to the neutral excitons. Both excitons A and B are within the bare energy and continuum, marked by arrows. The black curve is the experimental data [8], also shown as an enlarged manner in the inset. The frozen-atom approximated spectrum is shown in purple, while the spectrum corresponding to the independent-particle approximation under the RPA and local fields is shown by a green line. (b) The absorption spectra at different temperatures exhibiting a relative blueshifting of the peaks.

A is formed as a result of interband transitions from the V_1 valence energy band to the two lowest conduction bands C_1 and C_2 at K (K′) points in the BZ [Fig. 1(d)]. Similarly, exciton B is built due to the electronic transition from V_2 to C_1. The difference between these two excitonic peaks is exactly equal to the bare SoC valence bandwidth. Apart from these two peaks, the C exciton is located at 2.77 eV and is made from the deep-lying conduction and valence bands that take part in interband transitions resulting in a spectrally broad response, including contributions near the Γ point. The Eliashberg function can now be used to understand the coupling of the phonon modes with the three excitons. We now return to Figs. 2(c)–2(e), in which we computed the difference between the conduction and valence Eliashberg functions, and it is calculated for those bare states where the transition has taken place. For example, $V_1 \rightarrow C_1, C_2$ means the transition has occurred between the top valence band and the two lowest conduction bands (at K) [Fig. 1(d)], as is the case with the A exciton. The difference is then $\mathrm{Re}[g^2 F_{C_1}(\omega) - g^2 F_{V_1}(\omega)]$. This quantity, being a negative for semiconductors without any anomalous band-gap shrinkage with temperature, is found to be dominated mainly by the acoustic branches around 103 cm^{-1}. Out of these three, the LA branch is found to be the most significant, resulting in an in-plane torsional mode at K. The other acoustic branches contribute only to stretching of the lattice along the in-plane and out-of plane directions. A small peak around 255 cm^{-1} is due to the optical branch consisting of both in-plane (W atoms) and out-of-plane (Se atoms) torsional modes, but effective only by about 25% compared to the former. This is in stark contrast with that found in MoS_2 ML A-exciton buildup, where the main contribution comes from the optical branch around 400 cm^{-1} [27,51]. The B exciton couples in a similar manner, with a contribution of almost one-third from optical branches. A small addition can be seen coming from the midfrequency branch, and it is shown by a small peak around 194 cm^{-1}. Interestingly, the C exciton couples with both acoustic (around 116 cm^{-1}) as well as lower and higher optical branches (around 210 and 244 cm^{-1}) and is 70% more effective compared with the in-plane contribution. The effect of varying temperature on absorption spectra is shown in Fig. 5(b), where a higher redshifting of the absorption peaks is obtained. Analyzing carefully the intensity and broadening of excitons, we find that the B peaks more than A in the frozen-atom approximation (i.e., with only the G_0W_0 correction) and at 0 K. However, as the temperature increases, both peaks start to become smaller in magnitude. At all temperatures, the A peak is found to be slightly narrower than the B peak, but the spectra magnitude reduces more for the B exciton. Furthermore, both A and B excitons remain unchanged in terms of intensity, but there is a considerable broadening, especially for the B exciton. These results are in excellent agreement with the experimental results, where the PL intensity of the peaks contributing to the lower bound excitons A and B decreases with increasing temperature [52]. Here we could not capture the higher-lying exciton as demonstrated by Godde *et al.* [52], which follows an opposite trend with temperature after 110 K. This could be due to its existence as a result of the intervalley transition, which stands as a limitation in this current BSE execution. In their experiment, they studied the nature of all excitons and trions and found that only this higher-lying neutral exciton shows such an anomalous behavior with temperature. Additionally, they demonstrated that due to the dominance of this particular neutral exciton's intensity at higher temperatures, the integrated PL intensity (i.e., the sum of the contribution of all excitons and trions formed when the sample is exposed to light) shows an increasing trend with temperature, as also shown elsewhere [17]. All the other effects shown in this work, such as the redshift of the peaks in the absorption spectra with increasing temperature and the width of the peaks of the individual neutral excitons, follow the same trend as

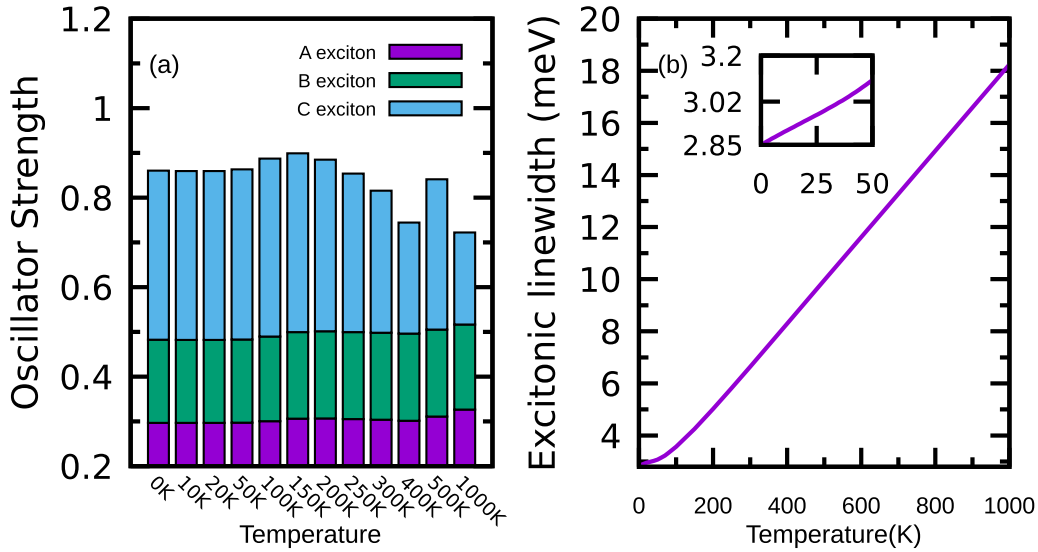

FIG. 6. (a) Exciton oscillator strengths at different temperatures. All the excitons are found to be bright at all temperatures. (b) *A*-excitonic nonradiative linewidths as a function of temperature. The inset enlarges a low-temperature variation.

demonstrated elsewhere [17,52]. The *C* exciton with its peak located at 2.77 eV is in good agreement with the reported experimental value spread about 2.5 eV [11]. A sight discrepancy in our results might be due to the use of a scissor operator in the BSE calculation that stretches the conduction and valence bands and therefore underestimates the energy coordinate of the higher-lying excitons. Nevertheless, we find that *C* behaves differently with increasing temperature, having its intensity reduced at a higher pace and its broadening increased considerably. In addition to these, the absorption spectra in the absence of a BS kernel (i.e., the independent-particle approximation) but including the static screening within the RPA have been plotted to compare the consequences on the peak positions.

The oscillator strengths of the three excitons over a range of temperatures are shown in Fig. 6(a). Excitons *A* and *B* are found to remain bright at all temperatures, whereas there is only a slight variation of the strength in the case of the *C* exciton in the range 250–1000 K. This can be understood from the first and second terms in Eq. (10). In the case when $|\varphi(T)\rangle \sim |\varphi_{\mathrm{FA}}\rangle$, the second term dominates and as a consequence there is an individual interaction that occurs between the phonons with electrons and holes. This is therefore the incoherent contribution and is the case with ML WSe_2. A bright to dark transition or vice versa would result in a nonzero but large value of the first term, and hence it is the coherent contribution. Such transitions occur due to the transfer of oscillator energies when a bundle of excitonic states get close, and they are found to dominate in *h*-BN [18]. As can be seen from Fig. 6(a), there are no excitonic states close in energy for *A*, *B*, or *C* excitons, hence there is no bright to dark transition or vice versa for any of the excitons. The *A*-excitonic nonradiative linewidth as a function of temperature is shown in Fig. 6(b). The residual linewidth at 0 K is found to be 2.85 meV. The linear section can be explained by fitting to the phonon-induced variation $\Upsilon(T) = \Upsilon_0(0) + \Upsilon' T$, where Υ' denotes the linear increase due to the acoustic phonons. An exponential variation would result in an exciton–optical-phonon interaction, which was recently found to be present in ML MoS_2 [53]. When extrapolated to 0 K, we find $\Upsilon_0(0) = 2.25$ meV. This is close to the value 1.6 ± 0.3 meV in the case of CVD-grown ML WSe_2 where the exciton-phonon interaction is mainly found to stem from acoustic modes [54]. Furthermore, we obtained the exciton–acoustic-phonon coupling strength $\Upsilon' = 15.6\ \mu\mathrm{eV\ K^{-1}}$. This is almost four times smaller than the CVD samples. The reason for these limitations in our results might be due to the ruling out of any defects in the lattice, exciton-exciton/trion interactions (i.e., the incorporation of higher-order Feynman diagrams and the formulation of a three-body time-dependent DFT Hamiltonian) as such. Interestingly, in Figs. 7(a) and 7(b) we have plotted the *A* and *C* excitonic wave functions at 300 K over the in-plane coordinates, respectively. The two-dimensional projection of the probability density of the excitonic states in both cases was calculated by fixing the hole position above the W atom at a distance of 1.05 Å. We took this distance since we found the electron density to be higher near the Se atoms, and it is also shown in the electron density plot (see Fig. S4 in the Supplemental Material [39]). Here the summation over all the states has been taken into account [19,55,56]. The spreading of the wave function of the *A* exciton is over a diameter of 31.60 Å and therefore envelops many unit cells. They are thus Wannier excitons. Moreover, the wave function appears to be spherically symmetric, suggesting that a 1*s* ground state, similar to that of the ground-state wave function of a hydrogen atom, is properly exhibited. The wave function of the *B* exciton is found to be of a similar nature and hence is not shown here. A rather more localized spreading with high binding energy of the *C* exciton is shown in Fig. 7(b), which spreads over a diameter of 26.56 Å. This spreading of the excitons is smaller than that of the ML MoS_2 obtained by *ab initio* results [27], confirming higher excitonic binding energies at room temperature in ML WSe_2. We understand that the inclusion of intervalley transitions explaining the intriguing spin as well as momentum-forbidden low-lying dark states together with thermal-expansion effects would have been much more accurate in describing the quenching of the PL spectra

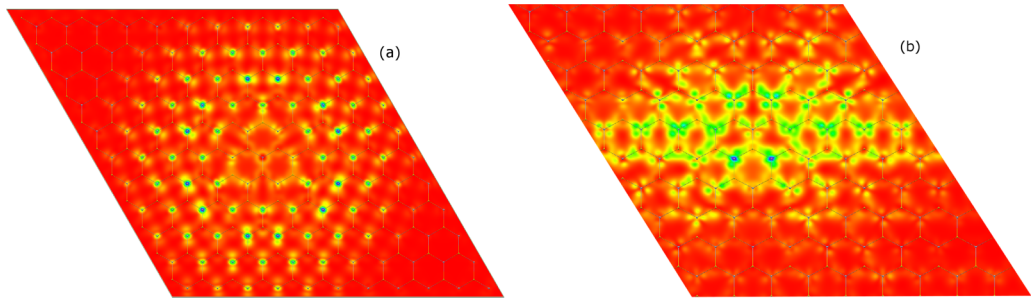

FIG. 7. Excitonic wave function plot at 300 K over the xy plane of the ML WSe_2. The hole is fixed in space and is placed on the top of the W atom at a distance of 1.05 Å. The wave function spreads to about (a) 31.60 Å over the entire plane in the case of the A exciton. For the C exciton (b), the spreading is brighter with a large oscillator strength and spreads only up to 26.56 Å.

at low temperatures. Such a computation would require a solution of the time-dependent BSE, and it is beyond the scope of this work. However, in this work we have presented an extensive quantitative analysis in order to understand the essential phonon couplings between the A, B, and C excitons. The role of lattice anharmonicities toward zero-point energies is also investigated.

IV. CONCLUSIONS

The lack of inversion symmetry and reduced screening in ML TMDCs plays a central role in building up a strong spin-orbit interaction hosting bound excitons with large binding energies. In this work, we demonstrate a contemporary and combined electron-electron, electron-hole, and electron-phonon study to reveal a thorough underlying mechanism of exciton-phonon couplings and energy renormalization in ML WSe_2. We use a complete *ab initio* formalism (starting from the bare energies) to explain the origin of neutral exciton-phonon couplings and the respective excitonic linewidths. The absorption and excitonic energies were obtained by solving the coupled electron-hole BSE that included the polaronic energies extracted from the DFPT calculations and are found to be in excellent agreement with the reported experimental data over a wide range of temperatures. Within this approach, we were able to capture features such as the oscillator strength of the excitonic peaks and their broadening, which directly related to the temperatures and to the nonradiative exciton relaxation time. Eliashberg functions were computed from these results and were analyzed against the phonon spectrum to understand the mode coupling of the electronic transitions between different energy bands about the optical gap. We found that the A and B excitons mainly couple with the LA phonons. The C exciton couples both with LA as well as optical modes near 225 cm^{-1}. Apparently, we also found that the electron-phonon interaction strongly renormalizes the bare electronic energies. To quantify the contributions from lattice anharmonicities, we executed a variable volume quasiharmonic analysis of the mode-dependent Grüneisen parameter along the BZ zone. This demonstrated that the out-of-plane mode contributes mostly to the lattice thermal contraction at lower temperature. In spite of this, we find that the effect of the lattice anharmonicities imparts many fewer energy corrections to the optical band gap compared with the electron-phonon interactions. We believe that this work would be a very useful reference to study the behavior of ML WSe_2-based excitonic solar cells at finite temperatures where the exciton physics governs the photoconversion.

ACKNOWLEDGMENTS

S.B. acknowledges financial support from the DST, India under Grant No. YSS/2015/000985 under Fast-Track Young Scientist Programme and Grant No. IFA 12-ENG-39 under INSPIRE Faculty Award Programme. H.M. and A.B. acknowledge MHRD and DST, Govt. of India, respectively, for providing fellowships.

APPENDIX: COMPUTATIONAL DETAILS

A unit cell of WSe_2 consisting of three atoms was first generated. The structure was truncated in the out-of-plane direction using a vacuum-slab-vacuum profile of 25 Å on each side to avoid the Coulombic interaction between repeated images. The PWSCF code [58] was then used to solve the Kohn-Sham equations. After testing the variety of kinetic cutoff energies, convergence was found to be achieved at 90 Ry for both atomic species [see Figs. S1(a) and S1(b) in the Supplemental Material [39]]. A Γ-centered Monkhorst-Pack scheme is then implemented for sampling the BZ with a dense grid of $18 \times 18 \times 1$. The structure was then allowed to relax within the variable cell configuration. The cell sizes as well as atomic coordinates were continuously updated along the minimum slope direction specified by the locally optimized coordinates calculated from the Hellmann-Feynman theorem. This minimizes the total energy of the unit cell with forces less than 10^{-4} eV $Å^{-1}$. A number of fully relativistic, norm-conserving pseudopotentials but with different exchange-correlation functionals were generated to realize the experimentally evaluated in-plane lattice constant, as shown in Table II. The same semicore-corrected orbitals were included

TABLE II. In-plane lattice parameter and band gap with various exchange functionals. Experimental lattice constant: 3.28 (Å) [57].

Exchange functionals	a (Å)	E_g (eV)
PZ	3.2468	1.387
PBE	3.3175	1.26
REVPBE	3.3365	1.217
BP	3.3333	1.2269

in all of these pseudopotentials. Among all others, we found the PBE exchange functional to correctly describe the relaxed in-plane lattice constant. A further optimization was done without varying the cell volume but within the same force limits. A two-spinor wave function was finally expanded in the plane-wave basis set along with a noncollinear and SoC calculation to carry out self-consistently evaluated charged densities. A non-self-consistently evaluated state calculation along the regular grid was finally done to interpolate the bare energy bands.

The excited-state computation was carried out by using the YAMBO code [59], and it involved a careful calculation of the QP energies with a dynamic dielectric screening function evaluated with the general plasmon-pole model. One of the two plasmon-pole frequencies was chosen to be 27.2 eV, beyond which the dielectric function remained unchanged. The exchange part in the static self-energy (Hartree-Fock) was summed over 20 065 **G**-vectors. A total of 150 bands, with the number of unoccupied bands 1.5 times the number of occupied bands, were used for summation of the polarization function [Eq. (7)]. The QP corrections were done in the lowest five empty conduction bands and the highest six valence bands along the BZ, and we were able to obtain a converged direct band gap of 2.19 eV in the G_0W_0 calculation. The energy cutoff for the response function was set to 5 Ry. An important ingredient was to manage the divergence of the Coulomb potential at small $\mathbf{q}$ appearing in the exchange as well as dynamic self-energies, BSE, etc. for reduced geometries. To fix this, a random integration method [59–61] was applied that assumes a smooth momenta integrand function (only for oscillators and occupation numbers) about $\mathbf{q}$ in each region of the BZ without changing the potential itself. For example, the diagonal matrix element of the exchange self-energy following this assumption can be written as $\langle n\mathbf{k}|\sum^{x}(\mathbf{r}_1,\mathbf{r}_2)|n\mathbf{k}\rangle \approx \sum_{\mathbf{q_i}}\sum_{\mathbf{G}} F(\mathbf{q_i},\mathbf{G})\int_{\mathrm{small_{BZ}}(\mathbf{q_i})} d^3\mathbf{q}\frac{4\pi}{|\mathbf{q}+\mathbf{G}|^2}$. This integral is evaluated using a numerical Monte Carlo method that resolves the $\mathbf{q}\to\mathbf{0}$ divergence, as the three-dimensional $\mathbf{q}$ integration prevents this from happening. In a similar way, the divergence associated with the electron-phonon Fan self-energy [Eq. (2)] can be evaluated from $\sum^{\mathrm{Fan}}_{n\mathbf{k}}(\omega) = \sum_{n'\mathbf{q}\lambda}\frac{|g^{\mathbf{q}\lambda}_{n'n\mathbf{k}}|^2}{N_q}[\frac{N(\omega_{\mathbf{q}\lambda})+1-f_{n'\mathbf{k}-\mathbf{q}}}{\omega-\epsilon_{n'\mathbf{k}-\mathbf{q}}-\omega_{\mathbf{q}\lambda}-i0^+}+\frac{N(\omega_{\mathbf{q}\lambda})+f_{n'\mathbf{k}-\mathbf{q}}}{\omega-\epsilon_{n'\mathbf{k}-\mathbf{q}}+\omega_{\mathbf{q}\lambda}-i0^+}]$. Note that here the number of $\mathbf{q}$ points is explicitly factored. To allow for the divergence at $\mathbf{q}\to\mathbf{0}$ of the $|g^{\mathbf{q}\lambda}_{n'n\mathbf{k}}|^2$ matrix elements and to speed up the convergence, the BZ is again divided into small regions (in the reciprocal lattice) centered around each $\mathbf{q}$ point. One can thus rewrite the Fan self-energy as $\sum^{\mathrm{Fan}}_{n\mathbf{k}}(\omega) = \sum_{\mathbf{q_i}}\sum_{n'\lambda}(\int_{\mathrm{small_{BZ}}(\mathbf{q_i})} d^3\mathbf{q}\frac{|g^{\mathbf{q}\lambda}_{n'n\mathbf{k}}|^2}{\Omega_{\mathrm{RL}}})[\frac{N(\omega_{\mathbf{q_i}\lambda})+1-f_{n'\mathbf{k}-\mathbf{q_i}}}{\omega-\epsilon_{n'\mathbf{k}-\mathbf{q_i}}-\omega_{\mathbf{q}\lambda}-i0^+}+\frac{N(\omega_{\mathbf{q_i}\lambda})+f_{n'\mathbf{k}-\mathbf{q_i}}}{\omega-\epsilon_{n'\mathbf{k}-\mathbf{q_i}}+\omega_{\mathbf{q}\lambda}-i0^+}]$. The integral $d^3\mathbf{q}$ is evaluated as $\int_{\mathrm{small_{BZ}}(\mathbf{q_i})} d^3\mathbf{q}\frac{|g^{\mathbf{q}\lambda}_{n'n\mathbf{k}}|^2}{\Omega_{\mathrm{RL}}} \approx \frac{|\mathbf{q_i}|^2|g^{\mathbf{q_i}\lambda}_{n'n\mathbf{k}}|^2}{\Omega_{\mathrm{RL}}}(\int_{\mathrm{small_{BZ}}(\mathbf{q_i})}\frac{d^3\mathbf{q}}{\mathbf{q}^2})$ using the Monte Carlo method. We see that in this case again the integral $\int_{\mathrm{small_{BZ}}(\mathbf{q_i})}\mathbf{q}^{-2}d^3\mathbf{q}$ does not blow up in the limit $\mathbf{q}\to\mathbf{0}$. In addition, the prefactor $|\mathbf{q_i}|^2|g^{\mathbf{q_i}\lambda}_{n'n\mathbf{k}}|^2$ is also regular when $\mathbf{q_i}\to\mathbf{0}$ [62]. 3 000 000 random points were incorporated in our calculation in order to evaluate the Coulomb integrals up to 100 **G**-vectors of the Coulomb potential in small BZ regions. The Monte Carlo technique was then used to evaluate this integral numerically defined within a box structure extending 25 Å on either side of the ML WSe_2. This truncated the Coulombic potential between the repeated images, and a faster convergence was achieved. A $12\times12\times1$ **k** sampling of the BZ was found to be sufficient for the evaluation of the Fan and Debye-Waller self-energies with a rigid self-consistent error threshold below 10^{-16} Ry and a single iteration mixing factor of 0.8 Ry that continuously updated ϕ_{scf}. Additionally, a phonon broadening of 1 meV is used in the analysis of the Eliashberg function to capture the phonon mode contributions. The polaronic and G_0W_0 corrections make the BS matrix non-Hermitian. Therefore, a full-diagonalization method is necessary to solve for the excitonic strengths and the lifetime, which included the top six valence bands and the five lowest conduction bands for the transitions. The value of the response block size is kept the same as in the case of the G_0W_0 calculation, i.e., 5 Ry, while the electric polarization vector direction was chosen to be normal to the plane of ML. The excitonic wave functions were then unfolded on the real-space lattice by using the XCRYSDEN code [63]. The variable volume QHA computations were performed on the same DFT charge-density results with the code developed by Dal Corso [58] under the same PWSCF code subroutines. The above configuration was found to be sufficient for optimizing the computational resources to the bare minimum, yet producing accurate results.

[1] A. Kogar, M. S. Rak, S. Vig, A. A. Husain, F. Flicker, Y. I. Joe, L. Venema, G. J. MacDougall, T. C. Chiang, E. Fradkin, J. van Wezel, and P. Abbamonte, Science **358**, 1314 (2017).

[2] A. Srivastava, M. Sidler, A. V. Allain, D. S. Lembke, A. Kis, and A. Imamoglu, Nat. Phys. **11**, 141 (2015).

[3] E. Navarro-Moratalla, J. O. Island, S. Mañas-Valero, E. Pinilla-Cienfuegos, A. Castellanos-Gomez, J. Quereda, G. Rubio-Bollinger, L. Chirolli, J. A. Silva-Guillén, N. Agraït, G. A. Steele, F. Guinea, H. S. J. van der Zant, and E. Coronado, Nat. Commun. **7**, 11043 (2016).

[4] K. Hao, G. Moody, F. Wu, C. K. Dass, L. Xu, C.-H. Chen, L. Sun, M.-Y. Li, L.-J. Li, A. H. MacDonald, and X. Li, Nat. Phys. **12**, 677 (2016).

[5] R. Suzuki, M. Sakano, Y. J. Zhang, R. Akashi, D. Morikawa, A. Harasawa, K. Yaji, K. Kuroda, K. Miyamoto, T. Okuda, K. Ishizaka, R. Arita, and Y. Iwasa, Nat. Nanotech. **9**, 611 (2014).

[6] N. Alidoust, G. Bian, S.-Y. Xu, R. Sankar, M. Neupane, C. Liu, I. Belopolski, D.-X. Qu, J. D. Denlinger, F.-C. Chou, and M. Z. Hasan, Nat. Commun. **5**, 4673 (2014).

[7] J. M. Riley, F. Mazzola, M. Dendzik, M. Michiardi, T. Takayama, L. Bawden, C. Granerød, M. Leandersson, T. Balasubramanian, M. Hoesch, T. K. Kim, H. Takagi, W. Meevasana, P. Hofmann, M. S. Bahramy, J. W. Wells, and P. D. C. King, Nat. Phys. **10**, 835 (2014).

[8] K. He, N. Kumar, L. Zhao, Z. Wang, K. F. Mak, H. Zhao, and J. Shan, Phys. Rev. Lett. **113**, 026803 (2014).

[9] Z. Ye, T. Cao, K. OB'rien, H. Zhu, X. Yin, Y. Wang, S. G. Louie, and X. Zhang, Nature (London) **513**, 214 (2014).

[10] G. Wang, X. Marie, I. Gerber, T. Amand, D. Lagarde, L. Bouet, M. Vidal, A. Balocchi, and B. Urbaszek, Phys. Rev. Lett. **114**, 097403 (2015).

[11] G. H. Ahn, M. Amani, H. Rasool, D.-H. Lien, J. P. Mastandrea, J. W. Ager III, M. Dubey, D. C. Chrzan, A. M. Minor, and A. Javey, Nat. Commun. **8**, 608 (2017).

[12] D. Le, A. Barinov, E. Preciado, M. Isarraraz, I. Tanabe, T. Komesu, C. Troha, L. Bartels, T. S. Rahman, and P. A. Dowben, J. Phys.: Condens. Matter **27**, 182201 (2015).

[13] J. S. Kin Fai Mak, K. He, and T. F. Heinz, Nat. Nanotech. **7**, 494 (2012).

[14] A. M. Jones, H. Yu, N. J. Ghimire, S. Wu, G. Aivazian, J. S. Ross, B. Zhao, J. Yan, D. G. Mandrus, D. Xiao, W. Yao, and X. Xu, Nat. Nanotech. **8**, 634 (2013).

[15] E. Poem, Y. Kodriano, C. Tradonsky, N. H. Lindner, B. D. Gerardot, P. M. Petroff, and D. Gershoni, Nat. Phys. **6**, 993 (2010).

[16] E. Malic, M. Selig, M. Feierabend, S. Brem, D. Christiansen, F. Wendler, A. Knorr, and G. Berghäuser, Phys. Rev. Mater. **2**, 014002 (2018).

[17] X.-X. Zhang, Y. You, S. Y. F. Zhao, and T. F. Heinz, Phys. Rev. Lett. **115**, 257403 (2015).

[18] A. Marini, Phys. Rev. Lett. **101**, 106405 (2008).

[19] A. Molina-Sánchez, D. Sangalli, K. Hummer, A. Marini, and L. Wirtz, Phys. Rev. B **88**, 045412 (2013).

[20] H. Shu, Y. Li, X. Niu, and J. Wang, ACS Appl. Mater. Interf. **8**, 13150 (2016).

[21] T. Galvani, F. Paleari, H. P. C. Miranda, A. Molina-Sánchez, L. Wirtz, S. Latil, H. Amara, and F. Ducastelle, Phys. Rev. B **94**, 125303 (2016).

[22] F. Karlický and M. Otyepka, J. Chem. Theor. Comput. **9**, 4155 (2013).

[23] G. Antonius, D. Y. Qiu, and S. G. Louie, Nano Lett. **18**, 1925 (2018).

[24] H. Y. Fan, Phys. Rev. **78**, 808 (1950).

[25] E. Cannuccia and A. Marini, Phys. Rev. Lett. **107**, 255501 (2011).

[26] F. Giustino, S. G. Louie, and M. L. Cohen, Phys. Rev. Lett. **105**, 265501 (2010).

[27] A. Molina-Sànchez, M. Palummo, A. Marini, and L. Wirtz, Phys. Rev. B **93**, 155435 (2016).

[28] E. Cannuccia, Ph.D. thesis, Rome Tor Vergata University (2011).

[29] M. Cardona, Sci. Technol. Adv. Mater. **7**, S60 (2005).

[30] G. D. Mahan, *Many-Particle Physics*, 3rd ed. (Springer International Edition, New York, 2014).

[31] C. E. Villegas, A. R. Rocha, and A. Marini, Nano Lett. **16**, 5095 (2016).

[32] N. Mounet and N. Marzari, Phys. Rev. B **71**, 205214 (2005).

[33] R. W. Godby and R. J. Needs, Phys. Rev. Lett. **62**, 1169 (1989).

[34] A. L. Fetter and J. D. Walecka, *Quantum Theory of Many-Particle Systems*, 1st ed. (Dover, Mineola, NY, 2013).

[35] L. Hedin, Phys. Rev **139**, A796 (1965).

[36] M. Rohlfing and S. G. Louie, Phys. Rev. B **62**, 4927 (2000).

[37] D. R. Hamann, Phys. Rev. B **88**, 085117 (2013).

[38] G. Antonius, S. Poncè, E. Lantagne-Hurtubise, G. Auclair, X. Gonze, and M. Côtè, Phys. Rev. B **92**, 085137 (2015).

[39] See Supplemental Material at http://link.aps.org/supplemental/10.1103/PhysRevB.98.045143 for brief description of materials.

[40] J. P. Echeverry, B. Urbaszek, T. Amand, X. Marie, and I. C. Gerber, Phys. Rev. B **93**, 121107(R) (2016).

[41] C. Zhang, Y. Chen, A. Johnson, M.-Y. L, L.-J. Li, P. C. Mende, R. M. Feenstra, and C.-K. Shih, Nano Lett. **15**, 6494 (2015).

[42] W.-T. Hsu, L.-S. Lu, D. Wang, J.-K. Huang, M.-Y. Li, T.-R. Chang, Y.-C. Chou, Z.-Y. Juang, H.-T. Jeng, L.-J. Li, and W.-H. Chang, Nat. Commun. **8**, 1 (2017).

[43] E. Cannuccia and A. Marini, Eur. Phys. J. B **85**, 320 (2016).

[44] D. Çakır, F. M. Peeters, and C. Sevik, Appl. Phys. Lett. **104**, 203110 (2014).

[45] L. D. Landau and E. M. Lifshitz, *Theory of Elasticity Volume 7: Course on Theoretical Physics*, 3rd ed. (Elsevier, Oxford, UK, 2010).

[46] X.-J. Ge, K.-L. Yao, and J.-T. Lü, Phys. Rev. B **94**, 165433 (2016).

[47] M. Yang, X. Cheng, Y. Li, Y. Ren, M. Liu, and Z. Qi, Appl. Phys. Lett. **110**, 093108 (2017).

[48] B. Monserrat and R. J. Needs, Phys. Rev. B **89**, 214304 (2014).

[49] G. Antonius, S. Poncé, P. Boulanger, M. Côtè, and X. Gonze, Phys. Rev. Lett. **112**, 215501 (2014).

[50] M. Grüning, A. Marini, and X. Gonze, Nano Lett. **9**, 2820 (2009).

[51] N. Saigal and S. Ghosh, Appl. Phys. Lett. **107**, 242103 (2015).

[52] T. Godde, D. Schmidt, J. Schmutzler, M. Aßmann, J. Debus, F. Withers, E. M. Alexeev, O. Del Pozo-Zamudio, O. V. Skrypka, K. S. Novoselov, M. Bayer, and A. I. Tartakovskii, Phys. Rev. B **94**, 165301 (2016).

[53] F. Cadiz, E. Courtade, C. Robert, G. Wang, Y. Shen, H. Cai, T. Taniguchi, K. Watanabe, H. Carrere, D. Lagarde, M. Manca, T. Amand, P. Renucci, S. Tongay, X. Marie, and B. Urbaszek, Phys. Rev. X **7**, 021026 (2017).

[54] G. Moody, C. K. Dass, K. Hao, C.-H. Chen, L.-J. Li, A. Singh, K. Tran, G. Clark, X. Xu, G. Berghaüser, E. Malic, A. Knorr, and X. Li, Nat. Commun. **6**, 8315 (2015).

[55] E. Ridolfi, C. H. Lewenkopf, and V. M. Pereira, Phys. Rev. B **97**, 205409 (2018).

[56] L. Wirtz, A. Marini, M. Grüning, C. Attaccalite, G. Kresse, and A. Rubio, Phys. Rev. Lett. **100**, 189701 (2008).

[57] J. Wilson and A. Yoffe, Adv. Phys. **18**, 193 (1969).

[58] P. Giannozzi, S. Baroni, N. Bonini, M. Calandra, R. Car, C. Cavazzoni, D. Ceresoli, G. L. Chiarotti, M. Cococcioni, I. Dabo, A. D. Corso, S. de Gironcoli, S. Fabris, G. Fratesi, R. Gebauer, U. Gerstmann, C. Gougoussis, A. Kokalj, M. Lazzeri, L. Martin-Samos, N. Marzari, F. Mauri, R. Mazzarello, S. Paolini, A. Pasquarello, L. Paulatto, C. Sbraccia, S. Scandolo, G. Sclauzero, A. P. Seitsonen, A. Smogunov, P. Umari, and R. M. Wentzcovitch, J. Phys.: Condens. Matter **21**, 395502 (2009).

[59] A. Marini, C. Hogan, M. Grüning, and D. Varsano, Comput. Phys. Commun. **180**, 1392 (2009).

[60] O. Pulcia, G. Onida, R. Del Sole, and L. Reining, Phys. Rev. Lett. **81**, 5374 (1998).

[61] C. A. Rozzi, D. Varsano, A. Marini, E. K. U. Gross, and A. Rubio, Phys. Rev. B **73**, 205119 (2006).

[62] E. Cannuccia and A. Marini, arXiv:1304.0072.

[63] A. Kokalj, Comput. Mater. Sci. **28**, 155 (2003).